REVIEW

Monolithic perovskite/c-Si tandem solar cell: Progress on numerical simulation

Chao Gao[1] , Daxue Du[1] and Wenzhong Shen[1,2]*

Abstract

Perovskite/c-Si tandem solar cell (TSC) has gradually become the hottest research topic in photovoltaic field for global carbon neutrality. Here we review the recent progress of numerical simulation studies of monolithic perovskite/c-Si TSC in terms of the methodology, light harvesting management, and energy yield aspects. It is summarized that the integration of physical fundamentals of the methodology, optimization of modeling and parameter correction can bring simulation results closer to experiments. Based on theoretical analysis of light harvesting management, we have demonstrated that textures can enhance light trapping capability and resonance absorption. The advances of bifacial perovskite/c-Si TSC have been particularly reviewed in simulation calibration (current matching loss approach) and low-cost strategy (ultrathin Si). Finally, through the energy yield analysis of the monofacial and bifacial TSC, we have innovatively proposed that spectral variables, effective albedo and top-cell bandgap should be integrated into cell preparation and module installation. This in-depth numerical simulation review provides a guidance for experimental preparation of low-cost and high-efficiency perovskite/c-Si TSC.

Keywords: Perovskite/c-Si, Numerical simulation, Methodology, Optical property, Energy yield

1 Introduction

As the most important branch of photovoltaic (PV) field for global carbon neutrality, crystalline silicon (c-Si) solar cell technology has a market share of over 95% due to the advantages of mature industry, low manufacturing cost and high material reliability. Currently, the research hotspots in the c-Si industry are focused on passivated emitter and rear cell (PERC), tunnel oxide passivated contact (TOPCon) cell and Si heterojunction (SHJ) cell. PERC has become the mainstream of the PV market since its conception in 1989 [1]. The power conversion efficiency (PCE) of the present mass production of p-Si PERCs is in the range of 22.8%–23.3% with the world-record PCE of 24.06% declared by Longi Solar (http://taiyangnews.info/technology/longi-24-06-efficiency-perc-cell-world-recod). TOPCon cell was first proposed by
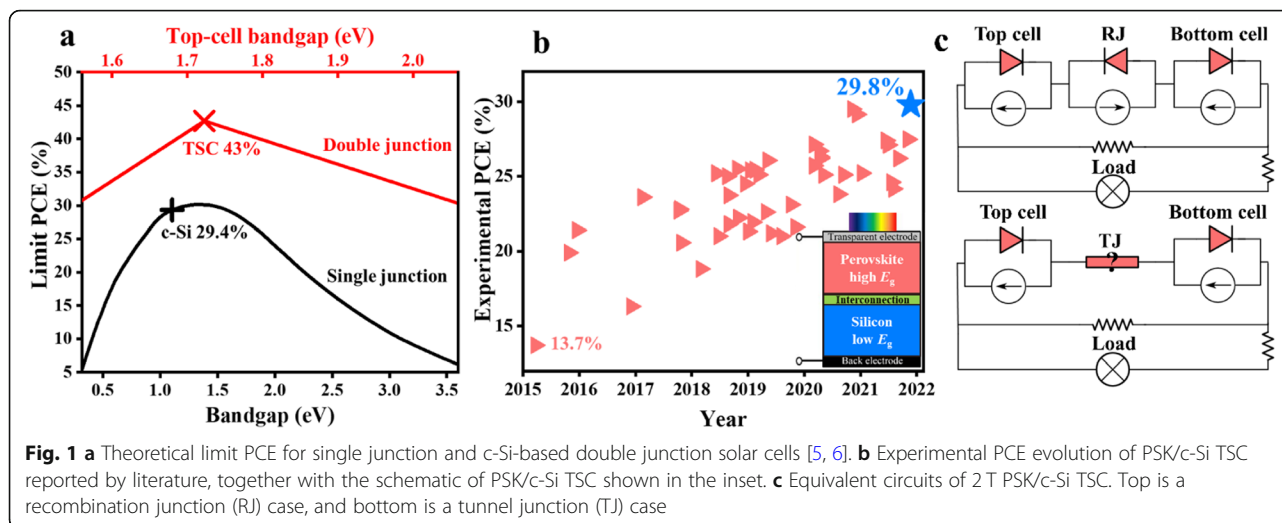
Feldmann et al. [2], in 2013, by using a passivated structure of ultrathin SiO_x and doped polycrystalline Si, thus achieving low recombination carrier selective contacts. Hollemann et al. [3], realized an efficiency of 26.1% utilizing a TOPCon structure in combination with an interdigitated back contact (IBC). SHJ cell is one of the most mature solar cells in the industry, and has been maintaining the world's highest efficiency in the field of c-Si cells due to its effective carrier selective contacts and heterojunction interface characteristics. Yoshikawa et al. [4], employed the SHJ structure combined with IBC electrodes to increase the efficiency to a certified 26.7%, which is currently the highest single junction non-concentrator c-Si solar cell in the world.

However, the PCE of c-Si solar cells is approaching the Shockley-Queisser limit (detailed balance) of 29.4% (Fig. 1(a)) [5], and the enhancement of single junction PCE will be very difficult due to the energy mismatched photons and the presence of electrical recombination (Auger, Shockley-Read-Hall, and etc.) [7]. The simplest way is to use absorber materials with different bandgaps to absorb photons of different energies, which can

* Correspondence: wzshen@sjtu.edu.cn
[1]Institute of Solar Energy, and Key Laboratory of Artificial Structures and Quantum Control (Ministry of Education), School of Physics and Astronomy, Shanghai Jiao Tong University, Shanghai 200240, People's Republic of China
[2]Collaborative Innovation Center of Advanced Microstructures, Nanjing 210093, People's Republic of China

Fig. 1 a Theoretical limit PCE for single junction and c-Si-based double junction solar cells [5, 6]. **b** Experimental PCE evolution of PSK/c-Si TSC reported by literature, together with the schematic of PSK/c-Si TSC shown in the inset. **c** Equivalent circuits of 2 T PSK/c-Si TSC. Top is a recombination junction (RJ) case, and bottom is a tunnel junction (TJ) case

reduce the thermal loss of high-energy electrons, and the most cost-effective approach is the 2-terminal perovskite/c-Si tandem solar cell (2 T PSK/c-Si TSC). According to numerical calculations by Yu et al. [6], (Fig. 1(a)) the theoretical tandem PCE can be as high as 43% using a PSK with a bandgap of 1.72 eV (experimental optimal bandgap of 1.68 eV) [8] in combination with a c-Si of 1.12 eV. As shown in Fig. 1(b) [8–50] (https://www.oxfordpv.com/), it takes only 6 years from the 13.7% (homojunction-based) first reported by Mailoa et al. [22], to 29.8% achieved by Helmholtz Zentrum Berlin (HZB) [50], revealing a very rapid progress in PCE of PSK/c-Si TSC. Moreover, based on the superiority of high PCE and mature industrialization of sub-cells, PSK/c-Si TSC has gradually become the hottest research topic in the field of multi-junction cells, and is expected to be a natural candidate for replacing conventional c-Si cells [51–53].

As a more widely used means of predicting the limit efficiency, the detailed balance makes the following assumptions: [54–56] (1) light absorption is assumed to be zero for the energy below the bandgap of the solar cell. All photons with energy above the bandgap are assumed to be absorbed; (2) each absorbed photon generates only one electron-hole pair; (3) the quasi-Fermi energy level is assumed to be constant; and (4) only recombination effect inside the solar cell is radiative recombination. For PSK solar cells, Sha et al. [54], exclusively revealed that the angularly unconstrained $MAPbI_3$ limit efficiency can reach 31%, and their dominant revelation of textured structure has been guiding the subsequent research work. To make the PSK photovoltaic performance close to the Shockley-Queisser limit, Zhang et al. [57], found that the 1-dimensional/3-dimensional (1D/3D) hybrid PSK films have significant

ferroelectricity, and learned from simulations that the PCE increases significantly with the increase of dielectric constant.

Since the direct connection between the PSK and Si devices will have a potential in the opposite direction, a recombination junction (RJ) or tunnel junction (TJ) is generally used to avoid the loss of open circuit voltage (V_{OC}), and its equivalent circuit is shown in Fig. 1(c). At present, the equivalent circuit of a RJ is unquestionable, but the TJ is modeled differently in special cases. With any reverse bias and a small forward bias, TJ is similar to a resistor. However, the TJ's behavior is dominated by thermionic emission under forward bias conditions when the current density is greater than the peak tunnel current [58]. This case requires the use of a thermionic-field emission expression based on the Wentzel-Kramers-Brillouin (WKB) approximation to simulate quantum tunnel effects.

Since PSK/c-Si TSC involves numerous functional interfaces (transparent electrodes, intermediate recombination layers, and transport layers), not only the fabrication process is complicated, but also its PV performance is affected by a combination of various factors. Experimentally screening the parameters of each layer is certainly the most straightforward method, but owing to the interactions among many parameters, it would be time-consuming and costly to study them separately. In this regard, photoelectric simulations allow to investigate each parameter independently, which makes it particularly significant. The specific effects of the parameters and the optimal cell structure obtained from the simulations can effectively guide the experimental process and achieve a novel breakthrough in PSK/c-Si TSC [59–63].

This invited review summarizes the progress of numerical simulation studies of PSK/c-Si TSC in terms of the methodology, light harvesting management, and

energy yield (*EY*) aspects. Starting with the physical fundamentals of the methodology, we outline five commonly used software kernels (finite element method (FEM) [64, 65], method of moments (MoM) [66], finite difference time domain (FDTD) [62, 63, 67–71], transfer matrix method (TMM) [72–75], and time domain integral equation (TDIE) [76]) for calculating electromagnetic problems, and point out that integration of methods, optimization of modeling and parameter correction can effectively improve simulation accuracy. For the light harvesting management part, by analyzing the optical properties of single junction cell, double junction cell and quasi-conformal structure, we illustrate that the textured PSK/c-Si TSC has excellent PV performance. A current matching loss (CML) method has also been introduced for bifacial PSK/c-Si TSC. For the *EY* part, we indicate that the root cause (weather, location, and time, etc.) affecting the *EY* of monofacial PSK/c-Si TSC is the spectral variables, and further for the bifacial issues, both the effective albedo and the PSK bandgap are to be considered. Hence, we conclude that it is essential to identify the intrinsic relevance of these factors and integrate them into cell preparation and module installation engineering to maximize *EY*. This in-depth numerical simulation review provides a guidance for experimental preparation of low-cost and high-efficiency PSK/c-Si TSC.

2 Physics and calculation methodology

There are a series of complex physical processes in solar cells from light incident to absorption and conversion into current [77–79], which can be roughly quantitatively described by the following eqs. (1)–(4).

$$\nabla \times (\nabla \times E) = k^2 \varepsilon_r E \tag{1}$$

$$\nabla \cdot \left[-D_n \nabla n + n\mu_n \left(\nabla \Psi + \frac{\nabla \chi}{q} + \frac{K_b T}{q} \nabla \ln N_C \right) - n D_{th}^n \nabla T \right] = G - U \tag{2}$$

$$\nabla \cdot \left[-D_p \nabla p - p\mu_p \left(\nabla \Psi + \frac{\nabla \chi}{q} + \frac{\nabla E_g}{q} - \frac{K_b T}{q} \nabla \ln N_V \right) - p D_{th}^p \nabla T \right] = G - U \tag{3}$$

$$\nabla^2 \Psi = \frac{q}{\varepsilon_0 \varepsilon_r} (n - p - C) \tag{4}$$

where E is electric field, k wave vector, ε_r the permittivity, D_n (D_p) the electron (hole) diffusion coefficient, n (p) the electron (hole) concentration, μ_n (μ_p) the electron (hole) mobility, Ψ the electrostatic potential, D^n_{th} (D^p_{th}) the electron (hole) thermal diffusion coefficient, χ the electron affinity, E_g the energy gap, N_C (N_V) the conduction (valence) band density of states, K_b the Boltzmann's constant, q the electron charge, T temperature, G the total generation rate, U the total recombination rate, ε_0 the initial permittivity, C the impurity concentration.

Equation (1) is the electromagnetic wave equation, which describes the propagation of photons in the solar cell under transverse electric (TE) and transverse magnetic (TM) incidence. The absorption spectrum and E can be accessed based on Eq. (1), and the G can be further derived through E and the imaginary part of the corresponding material permittivity [80, 81]. Therefore, the suitable anti-reflection layer and light trapping structures are usually designed to improve the effective light absorption and photocurrent of solar cells [18, 48]. However, the electron-hole pairs inside solar cells cannot fully generate current due to the existence of the U [77, 82, 83], commonly including radiation, Auger, Shockley-Read-Hall, and surface recombination. Poisson Eq. (4) handles with the problem of electric potential (V) distribution with the space charge density (J) into the cell, which can be solved according to the transport process of photons in solar cells after being absorbed as listed in the Eqs. (2) and (3). The *J-V* curve can be obtained by Eqs. (2–4) and the corresponding boundary conditions to find the maximum power point (MPP), then PV performance parameters (V_{OC}, short-circuit current density (J_{SC}), fill factor (*FF*), PCE) of solar cells can be solved according to existing procedures [62]. Similarly, the PV performance of bifacial single junction solar cells can be easily obtained by the addition of the absorption spectra under front and rear incidence.

Based on the aforementioned single junction solar cell characteristics, the PV performance of the PSK/c-Si TSC can be determined directly from that of its sub-cells. Since the current is required to be consistent in the series circuit, the current density of the bifacial tandem cell (J_{BT}) depends on the smaller one, and the open-circuit voltage of the bifacial tandem cell (V_{BT}) is sum of the sub-cells, as listed in Eqs. (5) and (6), respectively. Here, monofacial case is included in the bifacial PSK/c-Si TSC considered as a condition where the rear incidence is zero. It should be noted that many researchers regard the efficiency of the TSC as the sum of the efficiencies of the two sub-cells, which is only true when the currents of the two sub-cells are matched. In fact, the PCE of the bifacial tandem cell (PCE_{BT}) is less than the sum of the PCE of the two sub-cells due to the CML as described in Eq. (7) [84]. The CML establishes numerical relationships based on a strict energy balance principle and graphically analyzes the current characteristics of the sub-cell under bifacial illumination. This algorithm takes into account the effect of the mismatch current on the solar cell parameters, making the double junction more like a whole device (more accurate results). The PCE_{CML} can be directly acquired through MPP tracking from the *J-V* curves of the sub-cells by Eq.

(8). Hence, the fill factor of the bifacial tandem cell (FF_{BT}) can be easily obtained based on J_{BT}, V_{BT}, and PCE_{BT} by Eq. (9). Finally, the EY of the PSK/c-Si TSC is evaluated by Eq. (10) based on time-dependent spectral illuminate $P_{ill}(t)$.

$$J_{BT} = [J(top), J(bottom)]_{min} \tag{5}$$

$$V_{BT} = V(top) + V(bottom) \tag{6}$$

$$PCE_{BT} = PCE(top) + PCE(bottom) - PCE_{CML} \tag{7}$$

$$PCE_{CML} = \frac{[(J_{max} - J_{min})V_{max}]_{MPP}}{1000 \ W/m^2} \tag{8}$$

$$FF_{BT} = \frac{PCE_{BT}}{V_{BT} \cdot J_{BT}} \cdot 1000 \ W/m^2 \tag{9}$$

$$EY = \int P_{ill}(t) \cdot PCE_{BT} dt \tag{10}$$

The issue of light propagation and absorption in solar cells is ultimately a problem of solving electromagnetic field, for which there are many numerical methods, as shown in Table 1. The relatively mature kernels of simulation software are: FEM [64, 65], MoM [66], which belong to frequency domain technique; FDTD [62, 63, 67–71], TMM [72–75], and TDIE [76], which belong to time domain technique. Each method has its own features and limitations. Since MoM and TDIE only focus on electromagnetic scattering problems at surfaces and interfaces, they have no application in solar cell simulation. Currently, commonly used simulation software includes TCAD, GenPro4, JCMsuite, OPTOS, FDTD, SCAPS, and AFORS-HET. These are software packages written to simulate and optimize devices by combining already established optical models. Some software is integrated and contains both electrical and optical modules, such as Silvaco TCAD. Some dominant electrical simulation software is not applicable because the PSK/c-Si TSC requires a rigorous solution for the electromagnetic field due to its many structures and widely varying optical properties.

The optical simulation modules for solar cells are FEM, FDTD and TMM. Jäger et al. [64], utilized FEM combined with Lambertian law to provide an outlook on the light harvesting management of PSK/c-Si TSC and proposed excellent optical properties of the sinusoidal interface. The FEM discretizes the computational space into a finite number of small elements in the form of a sparse symmetric matrix, which is convenient for calculations. FEM is advanced for treating the interaction of light with complex structures, but may suffer from computational overload. Tennyson et al. [70], used FDTD to simulate the optical properties of textured PSK/c-Si TSC surfaces, and their results on the in/out-coupling of photons agree with the experimental photoluminescence (PL) characteristics. The FDTD takes Maxwell's equations as a starting point, with easy programming processing, short procedure development time, and more natural and explicit method logic. The computational area of FDTD can be either the cell interface or the interior of the structure, but too fine a mesh division can lead to a huge calculation. Bittkau et al. [72], applied TMM and genetic algorithm to analyze the optical loss of TSC each layer and give the optimal spectral structure and material design. The TMM principle is based on Huygens wave propagation model to calculate the light

Table 1 Overview of numerical calculation methods for electromagnetic fields

Technology	Methodology	Form	Characteristics	Refs.
Frequency Domain	**FEM**	Differential	Flexible discrete elements Sparse symmetric matrix facilitates the solution Accurate simulation for the interaction between the medium of complex structures and electromagnetic fields May require more storage space and computation time	[64, 65]
	MoM	Integral	Suitable for arbitrary shapes and non-uniformity problems Electromagnetic calculations limited to surfaces May lead to increased difficulty in solving very large matrices	[66]
Time Domain	**FDTD**	Differential	Using Maxwell's equations as a starting point Simulation of wave propagation and the interaction between light and matter in a computerized digital space Calculation area involves not only the surface, but also the interior Too fine a mesh can lead to a huge amount of calculations	[62, 63, 67–71]
	TMM	Differential	Huygens-based wave propagation model A method for calculating the propagation of light in multilayer films Complex multi-beam superimposed interference processes in matrix form Oversimplification of non-vertical incidence and multiple scattering	[72–75]
	TDIE	Integral	Accurate simulation calculations for surfaces and interfaces Post-storage of time to complete deferred integration, which greatly increases the storage time and space	[76]

in multilayer film, but simplifies non-vertical incidence and multiple scattering.

Current advances in optical simulation of tandem solar cells include: (1) integration of methods; (2) optimization of modeling; and (3) parameter correction. For the first progress, to address the restriction of single electromagnetic method, Liu et al. [85], proposed the optical path analysis combined with TMM to overcome the simulation difficulties of the metal shading and sub-band gap parasitic absorption. Besides making improvements manually, the simulation software can be an integration of multiple methods, such as matrix-based OPTOS [86–90] and GenPro4 [91, 92]. With the evolution of artificial intelligence, solar cell simulation may be combined with algorithms such as decision trees, genetic algorithms, logistic regression, and neural networks to generate easier and more accurate packages. For the second progress, the thickness of the Si bottom-cell in PSK/c-Si TSC is about 250 μm, the simulation computation is huge, and in order to reasonably allocate computer arithmetic power and resources, the infinite Si model is used for most modeling (only calculation of PSK and functional layers) [68, 69, 93]. To obtain more realistic results, Ba et al. [62], employed the bottom reflection integration method to deal with the computationally intensive problem of finite Si models. For the third progress, the current density mismatch becoming a regular occurrence in bifacial PSK/c-Si TSC, Du et al. [84], proposed the CML method to achieve correction of the simulation parameters to obtain more accurate results.

3 Light harvesting management
As experiments can be limited by various factors, theoretical aspects can pave the way for experimental studies. Numerical simulation is favored by many theorists as an important tool for analyzing scientific problems, and has numerous advantages [59–61, 94–96]. Firstly, the simulation can disassemble each structure of the cell to study the influence of each part independently, which helps to obtain the optimal detailed parameters in a comprehensive and detailed way. Second, simulations can investigate the effects of optical and electrical parameters on the overall performance of the cell, which can be combined with experiments to design better structural solutions and help improve the efficiency of experimental workers. Third, simulations allow the study for the experimental structure of advanced ideas.

3.1 Single junction solar cell
The laboratory certified efficiency of PSK single junction cells has increased from 3.8% [97] in 2009 to 25.5% [50, 98] currently, making it an ideal top-cell for TSC due to its bandgap tunability [99–101], high defect tolerance [102, 103], high absorption coefficient [104], and steep
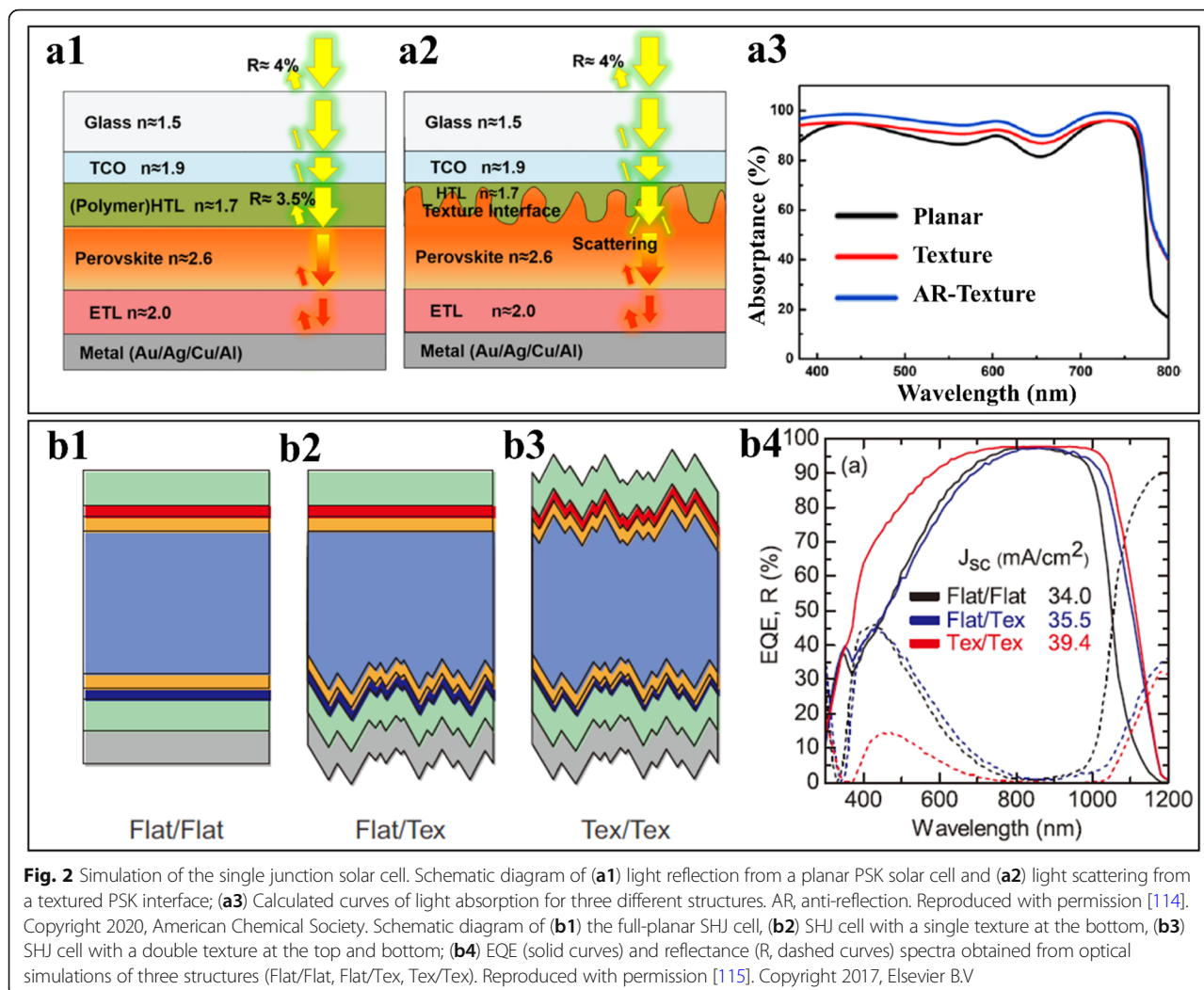
absorption edge [105–107]. The current study found that mirror-like PSK cells exhibit superior PV performance [108–111], contrary to the robust light trapping of pyramid-textured Si [112, 113]. To evaluate the effects of textured PSK interfaces on the light absorption, Xu et al. [114], utilized polystyrene spheres masked on the hole transport layer (HTL, 50 nm) to increase the roughness and reduce the reflection loss at the incident side. From the simulated results (Fig. 2(a1,2)), the average reflectance of the upper surface of the planar PSK reaches 3.5%, while the impact of reflection can be neglected at the textured interface due to the scattering effects. This finding is verified in Fig. 2(a3), the textured interface exhibits a high light absorption value, and is further enhanced after being coated with an anti-reflection (AR) film. Moreover, the results of these simulations are consistent with the experimental characterization in Ref. [114].

The production line process for c-Si solar cells commonly adopts a textured light incident surface to achieve optimal light capture [116–118]. To investigate the position specificity of the optical structure, Manzoor et al. [115], quantified and analyzed external quantum efficiency (EQE) loss by simulating the textured (Tex) interface at the top and bottom (Fig. 2(b1–3)). As shown in Fig. 2(b4), Tex/Tex has the highest EQE curve, and the integral J_{SC} of 34.0, 35.5, and 39.4 mA/cm^2 for Flat/Flat, Flat/Tex, and Tex/Tex, respectively, revealing the excellent spectral response of the textured structure. Furthermore, the waveband analysis of the EQE indicates that the bottom surface texture has a robust long-wave response and the top surface texture has a robust short-wave response, which agrees with the reflection (R) characteristics.

These simulations show that both PSK texture (nanoscale, achieved by etching 50 nm HTL) and c-Si texture (micron-scale, etching to produce about 2 μm pyramids) have strong light trapping ability, and these conclusions have been verified by experiments. However, the large-texture (micron-scale) can bring negative factors to the PSK film formation process, this can cause numerous defect states and electrical degradation. Therefore, while the inclusion of texture is beneficial, the control of size is particularly significant.

3.2 PSK/c-Si double junction solar cell
For a double junction solar cell, the building of PSK texture can be done with the optical structure of the c-Si bottom-cell, and the way of combining the structures of two different bandgap materials is the key to improve the efficiency of PSK/c-Si TSC. Due to the high experimental threshold for the preparation of different structures (e.g., textured PSK preparation involving dual-source co-evaporation) [8, 46–48], theoretical studies

Gao *et al. Carbon Neutrality*   (2022) 1:9

Page 6 of 16

Fig. 2 Simulation of the single junction solar cell. Schematic diagram of (**a1**) light reflection from a planar PSK solar cell and (**a2**) light scattering from a textured PSK interface; (**a3**) Calculated curves of light absorption for three different structures. AR, anti-reflection. Reproduced with permission [114]. Copyright 2020, American Chemical Society. Schematic diagram of (**b1**) the full-planar SHJ cell, (**b2**) SHJ cell with a single texture at the bottom, (**b3**) SHJ cell with a double texture at the top and bottom; (**b4**) EQE (solid curves) and reflectance (R, dashed curves) spectra obtained from optical simulations of three structures (Flat/Flat, Flat/Tex, Tex/Tex). Reproduced with permission [115]. Copyright 2017, Elsevier B.V
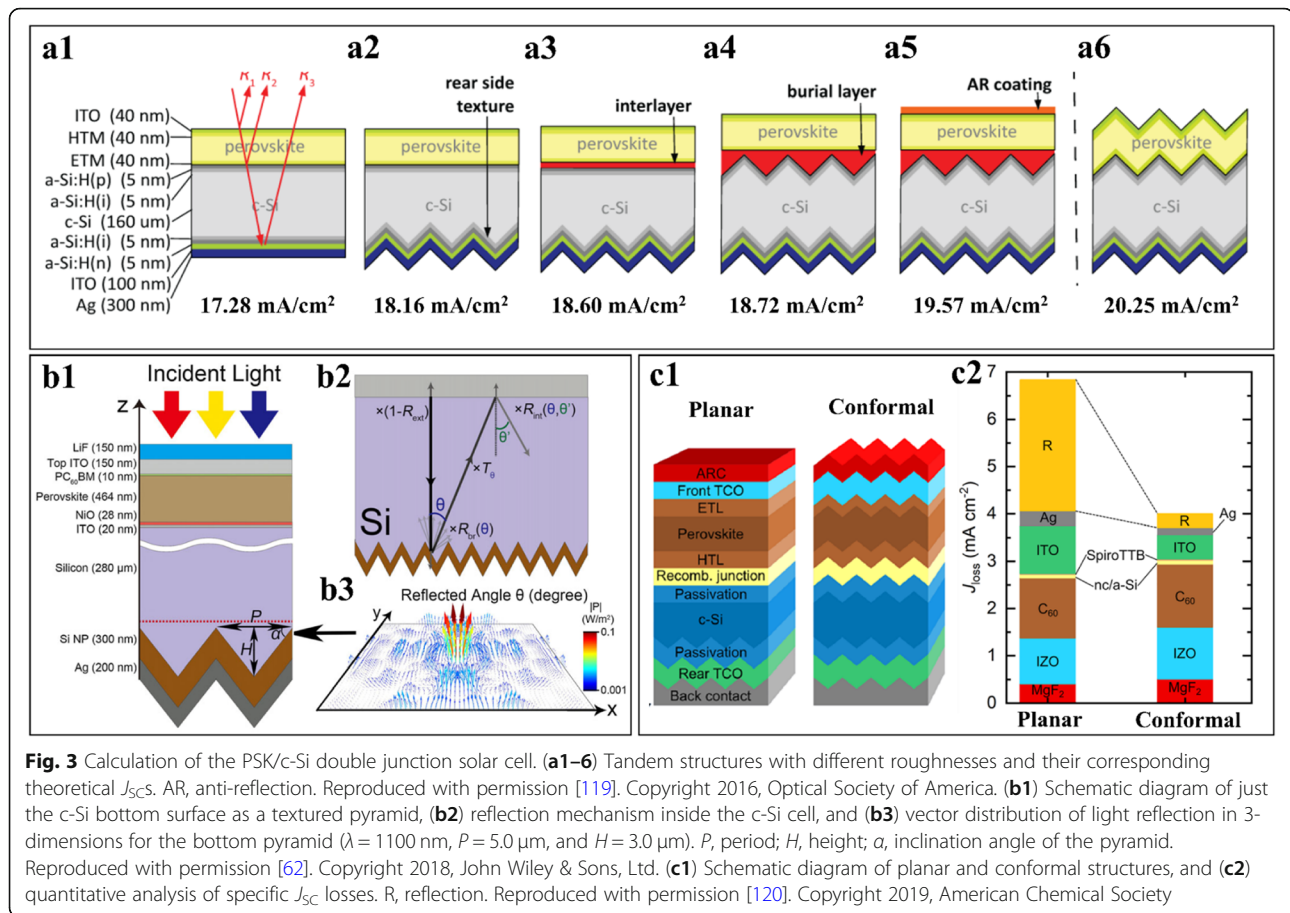
can provide guidelines for experiments to obtain the best solutions. As shown in Fig. 3(a1–6), Santbergen et al. [119], performed theoretical photocurrent density simulations for six structures using the TMM-based GenPro4 optical model. When textures are applied to the backside of the PSK/c-Si TSC (Fig. 3(a1,2)), the reflection loss is reduced and the current density (J_{SC}) increases from 17.28 to 18.16 mA/cm². When textures of the front and rear surfaces are designed (conformal structure, Fig. 3(a6)), the current density can be up to 20.25 mA/cm², which is the optimal theoretical structure for PSK/c-Si TSC. Since the exploitation of PSK is still in the planar stage, Santbergen et al. [119], gave three sets of planar PSK-based suboptimal tandem current densities from a theoretical viewpoint (Fig. 3(a3–5)): 18.60, 18.72, and 19.57 mA/cm². The loss of Fig. 3(a3) lies in the front surface reflection, the loss of Fig. 3(a4,5) originates from the parasitic absorption of the burial layer, and the anti-reflection (AR) layer of Fig. 3(a5) can promote the optical resonance effect and avoid the reflection. To

investigate the dominance of the TSC bottom texture, Ba et al. [62], utilized FDTD to simulate the light interaction at the bottom interface (Fig. 3(b1–3)). As the photons propagate to the bottom, the rough interface causes reflections in different directions and leads to an increase in current density due to the longer distance of the obliquely reflected light interacting inside c-Si. In addition, for the analysis of top texture advantage, Jacobs et al. [120], quantified the sources of optical loss in each aspect (MgF₂, IZO, C₆₀, and ITO, etc.) using TMM and Lambert-Beer's law (Fig. 3(c1,2)), where the greatest strength of the conformal structure over the planar structure is the significant reduction in reflection (R) loss. Therefore, the addition of both top and bottom textures can promote the light absorption of PSK/c-Si TSC and improve the PV performance.
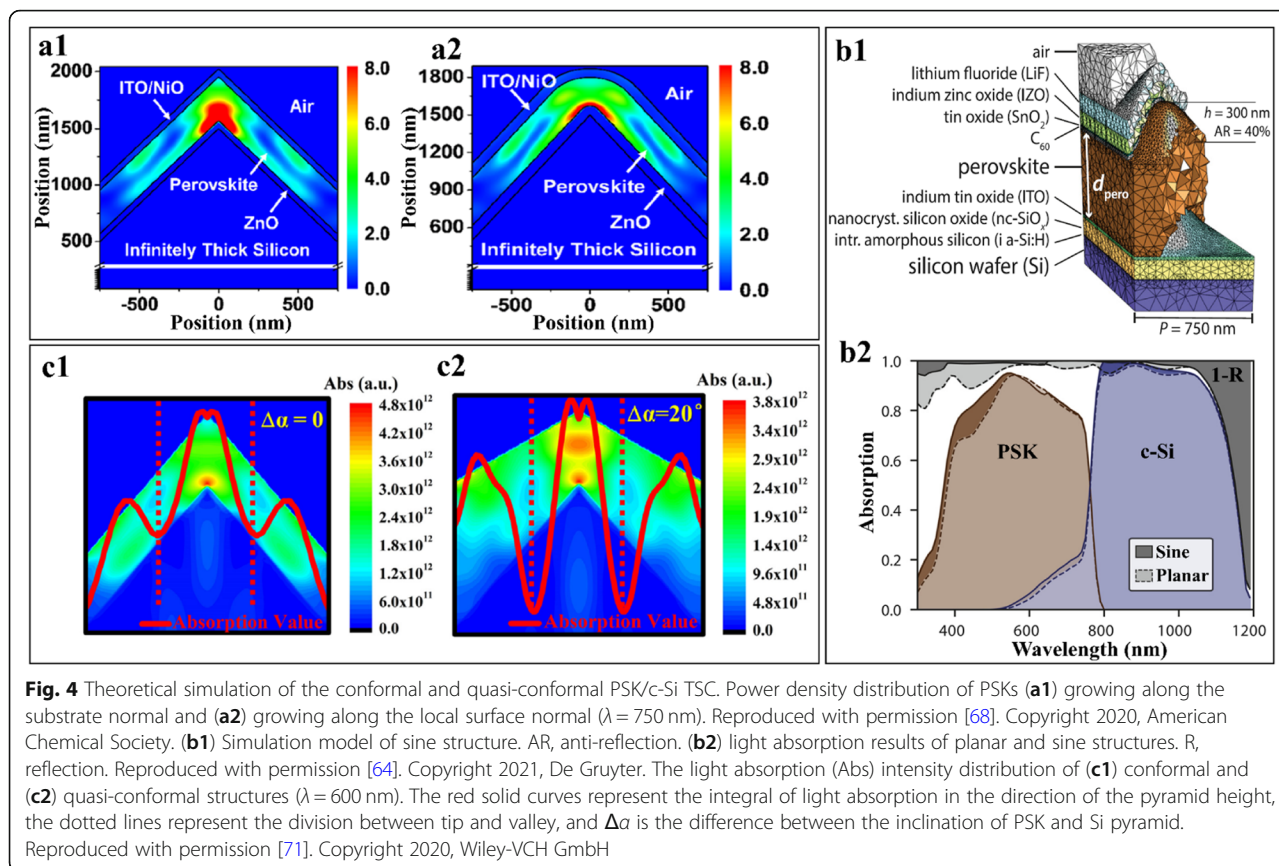
3.3 Quasi-conformal structures
Currently, the PSK preparation of conformal structure with dual-textures involves the complex dual-source co-

Fig. 3 Calculation of the PSK/c-Si double junction solar cell. (**a1–6**) Tandem structures with different roughnesses and their corresponding theoretical J_{SC}s. AR, anti-reflection. Reproduced with permission [119]. Copyright 2016, Optical Society of America. (**b1**) Schematic diagram of just the c-Si bottom surface as a textured pyramid, (**b2**) reflection mechanism inside the c-Si cell, and (**b3**) vector distribution of light reflection in 3-dimensions for the bottom pyramid ($\lambda = 1100$ nm, $P = 5.0$ μm, and $H = 3.0$ μm). P, period; H, height; a, inclination angle of the pyramid. Reproduced with permission [62]. Copyright 2018, John Wiley & Sons, Ltd. (**c1**) Schematic diagram of planar and conformal structures, and (**c2**) quantitative analysis of specific J_{SC} losses. R, reflection. Reproduced with permission [120]. Copyright 2019, American Chemical Society

evaporation and solution method with a laboratory efficiency of only 25.2% [48], while the fabrication of quasi-conformal structure (undulation of the interface is modified) is a facile one-step solution method and the tandem efficiency has been as high as 27.4% [43]. However, the experimental study of the quasi-conformal structure is only for the case where the front surface is flat (single-textured PSK) [39–43], so theoretical exploration of other types of interfaces in the quasi-conformal structure can understand the PV mechanism and extend the efficiency advantage of this structure. As shown in Fig. 4(a1,2), Qarony et al. [68], specifically investigated conformal and quasi-conformal structures using FDTD, in which the films grow along the substrate normal direction (SND) and along the local surface normal direction (LSND), respectively. By analyzing the power density distribution, they found that LSND can effectively attenuate the strong spot at the top of the pyramid compared with SND, and this effect can increase the effective light absorption thickness of PSK by 73%, which means the film deposition time can be reduced by 42%. Besides the curvature strategy on the upper surface of the quasi-conformal PSK, Jäger et al. [64],

utilized FEM to propose sinusoidal c-Si substrates to optimize the lower surface of the PSK. As shown in Fig. 4(b1,2), a Si substrate with a sinusoidal structure not only makes the growth of PSK easy, but it has a lower reflection in the short-wavelength range and a higher EQE value compared to the planar structure, indicating that the substrate optimization can achieve superior optical performance. To overcome the PSK coverage issues on the pyramidal texture, quasi-conformal PSK layers were prepared by Wang et al. [71], using starch additive engineering, and theoretical analysis was performed applying FDTD. As shown in Fig. 4(c1,2), the light absorption distribution becomes more uniform in the quasi-conformal structure ($\Delta a = 20°$), and it is found to have absorption enhancement in the valley by integrating over the height direction, which agrees with the results of Ref. [68]. These three methods of interfacial undulation modification (quasi-conformal structure), except for the preparation process to meet the requirements of PSK, can yield very similar optical properties to the conformal structure. As the experimental research of PSK/c-Si TSC advances, the quasi-conformal structure has gradually replaced the

Gao *et al. Carbon Neutrality*   (2022) 1:9

Page 8 of 16

Fig. 4 Theoretical simulation of the conformal and quasi-conformal PSK/c-Si TSC. Power density distribution of PSKs (**a1**) growing along the substrate normal and (**a2**) growing along the local surface normal ($\lambda = 750$ nm). Reproduced with permission [68]. Copyright 2020, American Chemical Society. (**b1**) Simulation model of sine structure. AR, anti-reflection. (**b2**) light absorption results of planar and sine structures. R, reflection. Reproduced with permission [64]. Copyright 2021, De Gruyter. The light absorption (Abs) intensity distribution of (**c1**) conformal and (**c2**) quasi-conformal structures ($\lambda = 600$ nm). The red solid curves represent the integral of light absorption in the direction of the pyramid height, the dotted lines represent the division between tip and valley, and Δa is the difference between the inclination of PSK and Si pyramid. Reproduced with permission [71]. Copyright 2020, Wiley-VCH GmbH

planar structure with severe optical loss and become the current hot spot in academia [44, 45].

3.4 Bifacial properties

To utilize the solar spectrum more efficiently, a bifacial strategy for solar cells will result in an increase in energy output of about 25% [121–123]. The concept of bifacial solar cells has now been widely employed in c-Si solar cells [124], and according to the International Technology Roadmap for Photovoltaic [125], market share of bifaciality is forecast to reach approximately 40% by 2028. The PSK/c-Si TSC with greater efficiency potential can take advantage of the c-Si backside, and besides receiving the solar spectrum from the front side, ground scattered and reflected light will allow the PCE of the bifacial TSC to be further enhanced (Fig. 5(a1)) [126]. As shown in Fig. 5(a2) [127], the lowest average albedo can reach 9% (sandstone), and the highest average albedo is even as high as 88% (snow), revealing that the solar irradiation on the back surface of the solar cell should not to be underestimated.

Since the experiment of PSK/c-Si TSC itself involves complex preparation and modulation of multilayers [46–48], coupled with the extremely high stability requirements for bifacial testing [41, 128, 129], the progress of the related bifacial studies is slow. Numerical

simulations can predict the actual benefits of the bifaciality in advance and give theoretical guidance to experimental studies. However, for the simulation of the bifacial PSK/c-Si TSC, previous reports have been performed without considering the effect of current mismatch on cell parameters [82, 130]. To address the effect of the albedo spectrum (Fig. 5(b1)), Du et al. [84], proposed the CML method to correct the simulation parameters and obtain more reliable results. As shown in Fig. 5(b2), when the bandgap of PSK is 1.55 eV, the difference in PCE of bifacial TSC (albedo 64%) relative to monofacial TSC (albedo 0%) is as high as 10.2% (absolute). When the albedo is 64%, the bifacial PCE of the TSC with a 1.75 eV PSK is 32.0%, while the bifacial PCE with a 1.55 eV PSK is up to 37.9%, reflecting the fact that the bifacial properties can lead to a smaller optimal bandgap (optimal bandgap of the monofacial PSK/c-Si TSC is 1.68 eV [8]). Furthermore, for the cost reduction and efficiency improvement of PSK/c-Si TSC, Du et al. [131], innovatively proposed to reduce the Si usage and achieve the redistribution of reflected light in the sub-cell by reducing the wafer thickness (Fig. 5(c1)). As shown in Fig. 5(c2), they applied FEM combined with CML to find that the 250 μm thickness c-Si bottom-cell has an advantage when the albedo is low, but when the albedo reaches about 35%,
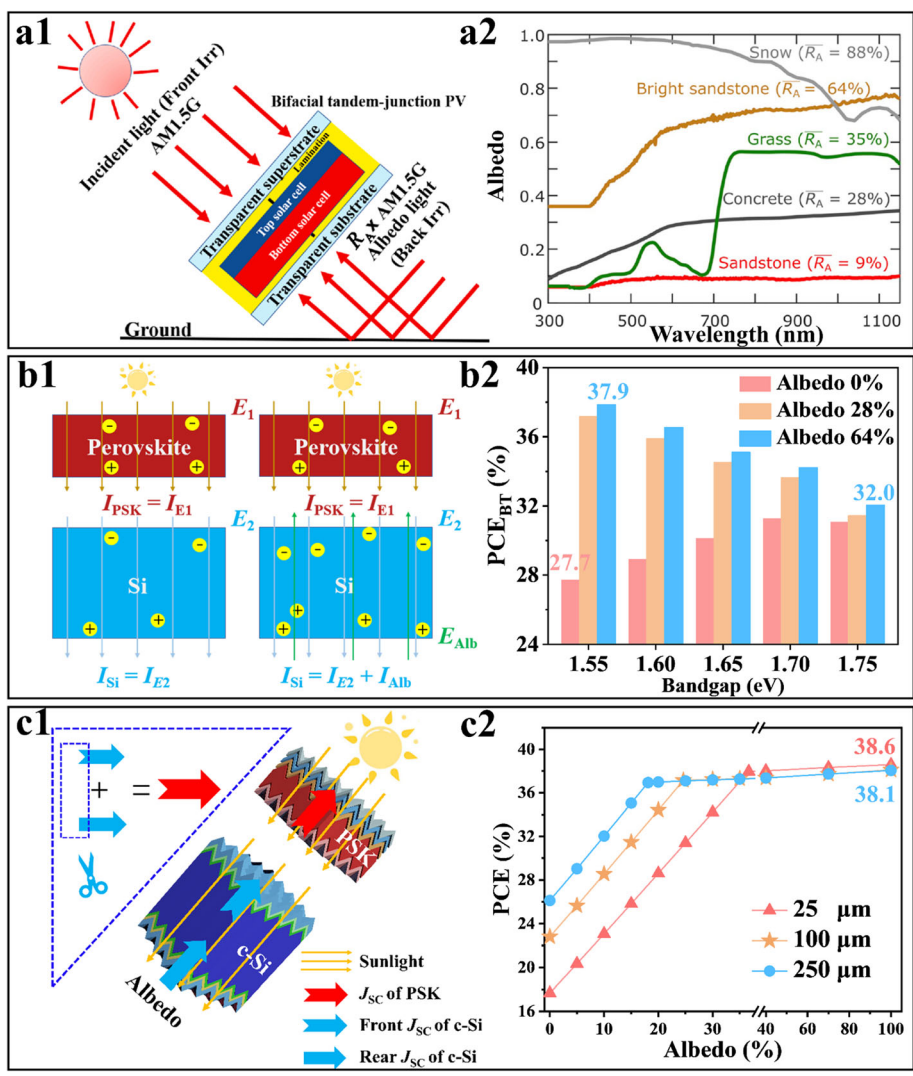
Fig. 5 Simulation of the bifacial PSK/c-Si TSC. (**a1**) Schematic diagram of the actual bifacial working environment. R_A, albedo; Irr, irradiance. Reproduced with permission [126]. Copyright 2021, Elsevier Ltd. (**a2**) Albedo curves formed by different types of ground. Reproduced with permission [127]. Copyright 2019, Elsevier B.V.. (**b1**) Principles of CML formation in a bifacial TSC, the left is monofacial TSC and the right is bifacial TSC. Alb, albedo. (**b2**) Calculated bifacial tandem (BT) efficiencies under different bandgaps and albedo conditions after CML correction. (**c1**) Diagram of ultrathin c-Si optimized for top-cell and bottom-cell current matching. (**c2**) TSC efficiencies obtained for three different thicknesses (25, 100, and 250 μm) of c-Si bottom-cells at various albedos

the tandem PCE is essentially the same for the three c-Si thicknesses (25, 100, and 250 μm). The tandem PCE of 25 μm c-Si is even as high as 38.6% when the albedo is 100%, revealing that the thinned Si strategy not only helps to reduce the cost, but also keeps the high PCE at sufficient albedos. These numerical researches can serve as a guidance for experimental preparation of low-cost and high-efficiency bifacial PSK/c-Si TSC.

4 Energy yield
Compared to a single junction solar cell, the currents of all sub-cells must be close to avoid current

mismatch as much as possible for a monolithically integrated TSC to obtain efficient *EY* [62, 132]. The angle of incidence and the intensity of the spectrum are often restricted by factors such as weather, location, and time under actual outdoor conditions [21, 67, 133–135], and the preparation of PSK with wide-bandgap is challenging, which limits the systematic study of *EY* in experimental work. On the contrary, numerical simulation is an efficient and feasible method to carry out in-depth exploration of these complex influencing factors, which is beneficial to formulate specific schemes for different scenarios to maximize the energy output.

4.1 Monofacial PSK/c-Si TSC

For monofacial properties, Jošt et al. [18], simulated two tilts of the building integrated photovoltaic (BIPV): 30° and 90° facing south in three cities (Washington, Golden, and Phoenix) located in the northern hemisphere. The annual *EY* of PSK/c-Si TSC for the two tilts are shown in Fig. 6(a1,2). Interestingly, 30° tilt always yields more *EY* than 90° tilts regardless of locations and cell types because of getting longer light time. And Phoenix yields the highest amount of energy more than 650 kWh/m² for the 30° tilt among three cities, but does not achieve a clear advantage for the 90° tilt due to a higher part of diffuse illumination. Analysis of the structures reveals that the *EY* of D (both-sided texture) is significantly higher than the other three structures (A (flat), B (back-sided texture), and C (back-sided texture + light management foil)), which reflects the superiority of the dual-textures, a conclusion that is consistent with Section 3.2. As we know, the light intensity and scattering intensity will be disturbed by location and weather and thus affect the performance of TSC. Futscher et al. [136], collected and compared solar irradiation of the Netherlands (Fig. 6(b1)) and Colorado (Fig. 6(b2)), which have the characteristics of oceanic climate and grassland climate, respectively. The measurement results show that the average photon energy (APE) of the

two places is close to the standard spectrum (AM1.5G, 1.845 eV). However, the annual average irradiance (249 W/m² in Netherlands and 432 W/m² in Colorado) is much lower than that of the standard spectrum (1000 W/m²). As shown in the inset of Fig. 6(b1), except for (1), which has a good match with AM1.5G, the solar irradiance spectra of the other cases ((2), (3), and (4)) vary tremendously, which means that the TSC current matching occurs only around data point 1. The J_{SC} has a weaker dependence on the APE, and the current-matched tandem is the most affected by spectral changes. The limiting efficiency of PSK/c-Si TSC varies greatly with time and location due to the variability of the spectrum, and the *EY* of tandem cells is even lower than that of single junction c-Si solar cells at high APEs and low irradiations. Similarly, Tucher et al. [137], exhibited hourly global irradiance with a tilt angle of 29° versus APE in Freiburg from January to December in Fig. 6(c1). Although the highest spectral irradiance occurs in the summer months corresponding to about 1.8 eV APE, there is a wide range of solar irradiation. As shown in Fig. 6(c2), the difference in the maximum PCE at different times even reaches about 20% (absolute), revealing that irradiation (spectral variables) is a significant factor affecting the *EY*.
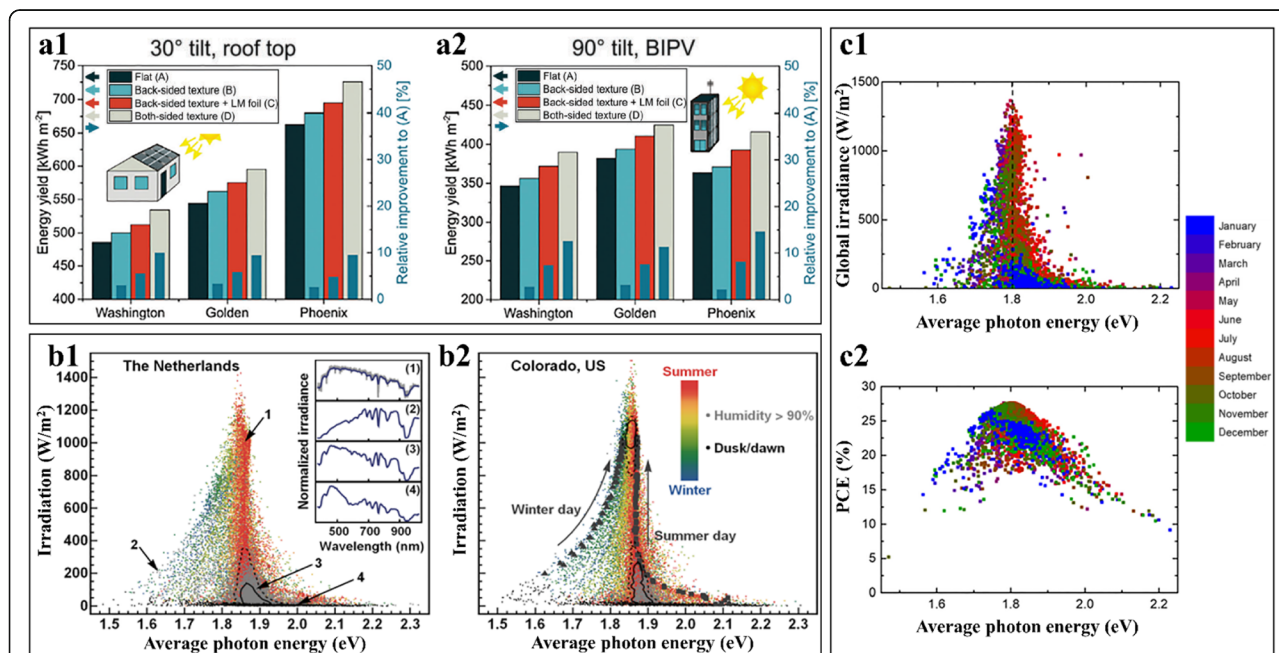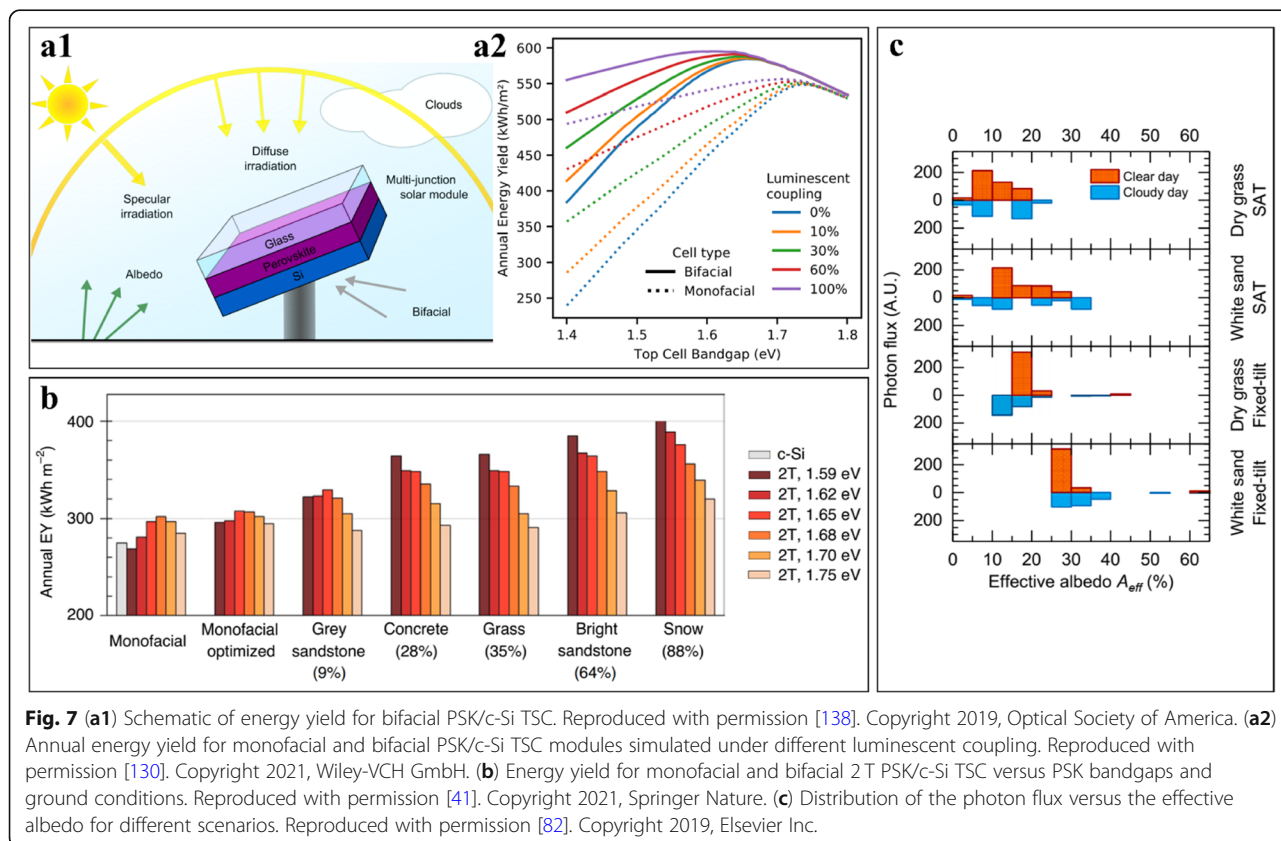

Fig. 6 Yearly energy yield for (**a1**) 30° and (**a2**) 90° solar cell orientation. Three different locations (Washington, Golden, and Phoenix) and four different cell types (A, B, C, and D) are compared here. LM, light management. Reproduced with permission [18]. Copyright 2018, The Royal Society of Chemistry. Solar spectral irradiance under the influence of weather in (**b1**) Netherlands and (**b2**) Colorado. The inset of (**b1**) illustrates the variation of the broad spectral distribution (1) at midday in summer with the standard spectrum (AM1.5G) in shades of gray, (2) during a winter morning, (3) during a summer day with high relative humidity, and (4) at dawn. The upright triangles and the squares in (**b2**) correspond to the course of clear sky days measured in winter and in summer, respectively. Reproduced with permission [136]. Copyright 2016, American Chemical Society. Time-dependent (**c1**) hourly global irradiance and (**c2**) PCEs of the PSK/c-Si TSC from January to December. Reproduced with permission [137]. Copyright 2019, Optical Society of America

4.2 Bifacial PSK/c-Si TSC

In comparison with the monofacial solar module, the bifacial one is interfered by more environmental factors including albedo due to the introduction of the rear incident light [84, 127, 138]. Fig. 7(a1) displays the *EY* modelling for the bifacial PSK/c-Si TSC varying with the location, incident orientation, weather, and albedo etc. Many studies have proved that rear incident photons cannot penetrate the c-Si sub-cell and be absorbed by the PSK layer [139, 140]. Therefore, the improvement of the current density of the c-Si sub-cell promotes the reduction of the optimized PSK bandgap under bifacial illumination, which leads to an increase in the current density of the bifacial PSK/c-Si TSC, thereby increasing the *EY*. In addition, as shown in Fig. 7(a2), Jäger et al. [130], found that the luminescent coupling between sub-cells has a similar effect to make the optimized PSK bandgap of the bifacial TSC red shift. In 2021, De Wolf team [41] firstly reported that the high-performance bifacial PSK/c-Si TSC with different PSK bandgaps achieved the *EY* of about 26 mW/cm^2 during outdoor testing. They performed annual *EY* simulations in Fig. 7(b) to assess the PV performance of monofacial and bifacial tandems under different PSK bandgaps and albedos. The highest *EY* was achieved with a PSK bandgap of 1.68 eV for monofacial structure and 1.59 eV for bifacial structure when the albedo exceeding 28%, and the *EY* of bifacial PSK/c-Si TSC has increased by more than 20% compared to a monofacial ones under the albedo supply. However, the increasing albedo has a weak gain in energy harvesting after achieving a matching albedo and PSK bandgap, which is also verified by the conclusions of Ref. [82]. To maximize the *EY* of bifacial PSK/c-Si TSC, Onno et al. [82], (Fig. 7(c)) investigated the relationship between photon flux and effective albedo. They found that in addition to the ground material (white sand and dry grass) itself causing albedo variations, single-axis tracking (SAT) has a wider distribution of photon flux compared to the fixed-tilt angle case. This means that for the bifacial TSC, the optimal bandgap PSK designed based on a certain albedo value deviates from its optimum at least part of the time in a SAT system, so the fixed-tilt may be the better solution. To ensure the reliability and lifetimes of solar cells, encapsulation is a common option. Currently, two encapsulation schemes (glass/glass and glass/transparent backsheet) combined with UV-curable adhesive technology are available in the market, which can provide a strong barrier to water and oxygen and effectively slow down the performance degradation.

Fig. 7 (**a1**) Schematic of energy yield for bifacial PSK/c-Si TSC. Reproduced with permission [138]. Copyright 2019, Optical Society of America. (**a2**) Annual energy yield for monofacial and bifacial PSK/c-Si TSC modules simulated under different luminescent coupling. Reproduced with permission [130]. Copyright 2021, Wiley-VCH GmbH. (**b**) Energy yield for monofacial and bifacial 2 T PSK/c-Si TSC versus PSK bandgaps and ground conditions. Reproduced with permission [41]. Copyright 2021, Springer Nature. (**c**) Distribution of the photon flux versus the effective albedo for different scenarios. Reproduced with permission [82]. Copyright 2019, Elsevier Inc.

Gao *et al. Carbon Neutrality*   (2022) 1:9

Page 12 of 16

5 Summary and outlook

In this review, we have summarized the physics and calculation methodologies, and concluded the research progress on both the light harvesting management and *EY* topics of the 2 T PSK/c-Si TSC. We start from the physical equations of light-medium interaction, Poisson equation, and the PV parameters calculation of double junction solar cell. Through the analysis of numerical methodologies, we conclude that a single electromagnetic calculation software kernel (FEM, MoM, FDTD, TMM, or TDIE) is very limited to deal with the problem, and the integration of methods can optimize the allocation of computational resources and thus improve the arithmetic power. The optimization of modeling and the parameter correction greatly improve the accuracy of the simulation. However, due to the many fields of physics, energy and computers involved in PSK/c-Si TSC simulation, every progress is a struggle. In the future, the development of advanced integrated software packages based on artificial intelligence, which will revolutionize the impact on numerical simulation.

For the analysis of the optical properties, we point out that the textured structure induces photon coupling to enhance the light trapping capability, so the addition of textures is beneficial for the improvement of PV performance in both single junction and double junction cells. For the conformal PSK preparation of TSC involving a complex co-evaporation process, we realize that the quasi-conformal structure can achieve optical gain, while maintaining the simplicity advantage of the one-step solution method. Nevertheless, the relevant quasi-conformal structures mentioned in this review are theoretical models, sine and LSND cannot be implemented experimentally (only single-textured PSK with a maximum PCE = 27.4% has been achieved in the laboratory), so it is full of challenges and opportunities from structural design to experimental completion.

To address the effects caused by the albedo spectrum in the bifacial PSK/c-Si TSC, we present the CML calculation method, which allows the current mismatch to be fully considered. It is found by CML simulations that when the albedo is sufficient (albedo > 35%), the tandem PCE of c-Si with 25 μm thickness is not substantially different from that of 250 μm. Although this ultrathin c-Si scheme can effectively reduce the cost of solar cells, silver paste cost and equipment availability are still important factors restricting the industrialization of PSK/c-Si TSC. If these economic issues are resolved, the levelized cost of electricity for PSK/c-Si TSC will be lower, which will result in lower prices on the grid.

Focusing on the simulation part of *EY*, our analysis shows that the spectral variables are the essence of the constraints on *EY* except for the illumination time and the intrinsic PCE (AM1.5G, under current-matched conditions). For *EY* of bifacial PSK/c-Si TSC, the issue of optimal bandgap of PSK and the effect of effective albedo on current density need to be taken into account more. According to Ref. [41], although the 1.68 eV PSK is regarded as the optimal bandgap for monofacial case, the annual *EY* of 1.59 eV PSK (bifacial TSC) is more than 20% higher than that of 1.68 eV PSK (monofacial TSC) when the albedo exceeds 28%. In order to obtain the maximum *EY*, the current mismatch had to be handled before PSK/c-Si TSC preparation and module installation. Nonetheless, under outdoor conditions, the solar spectrum and effective albedo change all the time, which means that the current mismatch cannot be fundamentally eliminated, so application-based experimental testing cannot be limited to standard conditions either. The spectrum sharing of the sub-cell directly determines the current matching, so we can achieve the maximum utilization of the spectrum from three directions: (1) bandgap and thickness of PSK, (2) solar spectral variables, and (3) effective albedo. In summary, with the deepening of investigation, we believe that PSK/c-Si TSC can definitely lead the solar cell industrialization as a low-cost *EY* device in the future.

The industrial production of PSK/c-Si TSC cannot be separated from stability. For experimental investigations, Kim et al. [20], (2020) maintained 80% of the initial tandem PCE (20.7%) by using an anion-engineered 2D additive at the 3D PSK grain boundaries, even after 1000 h of continuous illumination. Further, Li et al. [141], (2021) achieved a great breakthrough in stability by constructing a gradient PSK thin layer, and the PCE declined by only absolute 1.41% over 10,000 h. On the theoretical level, while ion migration models are important tools for understanding the photovoltaic performance of planar PSK, simple models of single junction are no longer applicable to face the complex architectures and textured interfaces in the PSK/c-Si TSC. Hence, taking into account the configuration of the PSK/c-Si TSC and even the potential induced degradation (PID) of the Si solar cell is a natural choice for a proper understanding of PSK/c-Si TSC stability in the future.

Authors' contributions

The manuscript was written through contributions of all authors. CG carried out literature investigation and screening, and wrote this review. DXD wrote parts of the manuscript and provided suggestions. WZS conceived the project and made significant contributions to the revision of the paper. The author(s) read and approved the final manuscript.

Authors' information

Chao Gao received his B.S. degree in School of Physics and Materials Science from Anhui University, China, in 2019. Currently, he is a Ph.D. candidate at School of Physics and Astronomy, Shanghai Jiao Tong University. His research interests include the solar energy materials, optical structure and perovskite/crystalline silicon tandem solar cell.
Daxue Du received his B.S. degree in Qinghai University, China, in 2016. Currently, he is a Ph.D. at School of Environment and Chemical Engineering, Yanshan University. He is involved in a joint program between Yanshan University and Shanghai Jiao Tong University. His research interests include light management of crystalline silicon and its tandem solar cell.
Wenzhong Shen received his Ph.D. degree in semiconductor physics and semiconductor device from Shanghai Institute of Technical Physics, Chinese Academy of Sciences, in 1995. Since 1999, Dr. Shen has been with Shanghai Jiao Tong University, China, as a full professor in the School of Physics and Astronomy, where he is currently the director of Institute of Solar Energy and Key Laboratory of Artificial Structures and Quantum Control, Ministry of Education.

Funding

Availability of data and materials

All data generated or analyzed during this study are included in this article.

Declarations

Ethics approval and consent to participate

Not applicable.

Consent for publication

Written informed consent for publication was obtained from all participants.

Competing interests

The authors declare no conflict of interest.

References

1. Green MA (2015) The passivated emitter and rear cell (PERC): from conception to mass production. Sol Energy Mater Sol Cells 143:190–197. https://doi.org/10.1016/j.solmat.2015.06.055
2. Feldmann F, Bivour M, Reichel C et al (2014) Passivated rear contacts for high-efficiency n-type Si solar cells providing high interface passivation quality and excellent transport characteristics. Sol Energy Mater Sol Cells 120:270–274. https://doi.org/10.1016/j.solmat.2013.09.017
3. Hollemann C, Haase F, Schäfer S et al (2019) 26.1%-efficient POLO-IBC cells: quantification of electrical and optical loss mechanisms. Prog Photovoltaics 27:950–958. https://doi.org/10.1002/pip.3098
4. Yoshikawa K, Kawasaki H, Yoshida W, Irie T, Konishi K, Nakano K, Uto T, Adachi D, Kanematsu M, Uzu H, Yamamoto K (2017) Silicon heterojunction solar cell with interdigitated back contacts for a photoconversion efficiency over 26%. Nat Energy 2(5):17032. https://doi.org/10.1038/nenergy.2017.32
5. Shockley W, Queisser HJ (1961) Detailed balance limit of efficiency of p-n junction solar cells. J Appl Phys 32:510–519. https://doi.org/10.1063/1.1736034
6. Yu Z, Leilaeioun M, Holman Z (2016) Selecting tandem partners for silicon solar cells. Nat Energy 1:16137. https://doi.org/10.1038/nenergy.2016.137
7. Hirst LC, Ekins-Daukes NJ (2011) Fundamental losses in solar cells. Prog Photovoltaics 19(3):286–293. https://doi.org/10.1002/pip.1024
8. Aydin E, Allen TG, De Bastiani M et al (2020) Interplay between temperature and bandgap energies on the outdoor performance of perovskite/silicon tandem solar cells. Nat Energy 5:851–859. https://doi.org/10.1038/s41560-020-00687-4
9. Al-Ashouri A, Kohnen E, Li B et al (2020) Monolithic perovskite/silicon tandem solar cell with > 29% efficiency by enhanced hole extraction. Science 370:1300–1309. https://doi.org/10.1126/science.abd4016
10. Albrecht S, Saliba M, Baena JPC et al (2016) Monolithic perovskite/silicon-heterojunction tandem solar cells processed at low temperature. Energy Environ Sci 9:81–88. https://doi.org/10.1039/c5ee02965a
11. Bett AJ, Schulze PSC, Winkler KM, Kabakli ÖS, Ketterer I, Mundt LE, Reichmuth SK, Siefer G, Cojocaru L, Tutsch L, Bivour M, Hermle M, Glunz SW, Goldschmidt JC (2020) Two-terminal perovskite silicon tandem solar cells with a high-bandgap perovskite absorber enabling voltages over 1.8 V. Prog Photovoltaics 28(2):99–110. https://doi.org/10.1002/pip.3208
12. Bush KA, Manzoor S, Frohna K, Yu ZJ, Raiford JA, Palmstrom AF, Wang HP, Prasanna R, Bent SF, Holman ZC, McGehee MD (2018) Minimizing current and voltage losses to reach 25% efficient monolithic two-terminal perovskite-silicon tandem solar cells. ACS Energy Lett 3(9):2173–2180. https://doi.org/10.1021/acsenergylett.8b01201
13. Bush KA, Palmstrom AF, Yu ZJ et al (2017) 23.6%-efficient monolithic perovskite/silicon tandem solar cells with improved stability. Nat Energy 2: 17009. https://doi.org/10.1038/nenergy.2017.9
14. Chen B, Yu Z, Liu K et al (2019) Grain engineering for perovskite/silicon monolithic tandem solar cells with efficiency of 25.4%. Joule 3:177–190. https://doi.org/10.1016/j.joule.2018.10.003
15. Fan R, Zhou N, Zhang L et al (2017) Toward full solution processed perovskite/si monolithic tandem solar device with pce exceeding 20%. Sol RRL 1:1700149. https://doi.org/10.1002/solr.201700149
16. Hou F, Han C, Isabella O et al (2019) Inverted pyramidally-textured PDMS antireflective foils for perovskite/silicon tandem solar cells with flat top cell. Nano Energy 56:234–240. https://doi.org/10.1016/j.nanoen.2018.11.018
17. Hou F, Yan L, Shi B et al (2019) Monolithic perovskite/silicon-heterojunction tandem solar cells with open-circuit voltage of over 1.8 V. ACS Appl Energy Mater 2:243–249. https://doi.org/10.1021/acsaem.8b00926
18. Jošt M, Koehnen E, Morales-Vilches AB et al (2018) Textured interfaces in monolithic perovskite/silicon tandem solar cells: advanced light management for improved efficiency and energy yield. Energy Environ Sci 11:3511–3523. https://doi.org/10.1039/c8ee02469c
19. Kim CU, Yu JC, Jung ED et al (2019) Optimization of device design for low cost and high efficiency planar monolithic perovskite/silicon tandem solar cells. Nano Energy 60:213–221. https://doi.org/10.1016/j.nanoen.2019.03.056
20. Kim D, Jung HJ, Park IJ et al (2020) Efficient, stable silicon tandem cells enabled by anion-engineered wide-bandgap perovskites. Science 368:155–160. https://doi.org/10.1126/science.aba3433
21. Koehnen E, Jost M, Morales-Vilches AB et al (2019) Highly efficient monolithic perovskite silicon tandem solar cells: analyzing the influence of current mismatch on device performance. Sustain Energy Fuels 3:1995–2005. https://doi.org/10.1039/c9se00120d
22. Mailoa JP, Bailie CD, Johlin EC et al (2015) A 2-terminal perovskite/silicon multijunction solar cell enabled by a silicon tunnel junction. Appl Phys Lett 106:121105. https://doi.org/10.1063/1.4914179
23. Mazzarella L, Lin Y-H, Kirner S et al (2019) Infrared light management using a nanocrystalline silicon oxide interlayer in monolithic perovskite/silicon heterojunction tandem solar cells with efficiency above 25%. Adv Energy Mater 9:1803241. https://doi.org/10.1002/aenm.201803241
24. Qiu Z, Xu Z, Li N, Zhou N, Chen Y, Wan X, Liu J, Li N, Hao X, Bi P, Chen Q, Cao B, Zhou H (2018) Monolithic perovskite/Si tandem solar cells exceeding 22% efficiency via optimizing top cell absorber. Nano Energy 53:798–807. https://doi.org/10.1016/j.nanoen.2018.09.052
25. Sahli F, Kamino BA, Werner J, Bräuninger M, Paviet-Salomon B, Barraud L, Monnard R, Seif JP, Tomasi A, Jeangros Q, Hessler-Wyser A, de Wolf S, Despeisse M, Nicolay S, Niesen B, Ballif C (2018) Improved optics in monolithic perovskite/silicon tandem solar cells with a nanocrystalline silicon recombination junction. Adv Energy Mater 8(6):1701609. https://doi.org/10.1002/aenm.201701609
26. Schulze PSC, Bett AJ, Bivour M et al (2020) 25.1% high-efficiency monolithic perovskite silicon tandem solar cell with a high bandgap perovskite absorber. Sol RRL 4:2000152. https://doi.org/10.1002/solr.202000152

27. Shen H, Omelchenko ST, Jacobs DA, Yalamanchili S, Wan Y, Yan D, Phang P, Duong T, Wu Y, Yin Y, Samundsett C, Peng J, Wu N, White TP, Andersson GG, Lewis NS, Catchpole KR (2018) In situ recombination junction between p-Si and TiO₂ enables high-efficiency monolithic perovskite/Si tandem cells. Sci Adv 4(12):9711. https://doi.org/10.1126/sciadv.aau9711

28. Werner J, Walter A, Rucavado E et al (2016) Zinc tin oxide as high-temperature stable recombination layer for mesoscopic perovskite/silicon monolithic tandem solar cells. Appl Phys Lett 109:233902. https://doi.org/10.1063/1.4971361

29. Werner J, Weng CH, Walter A et al (2016) Efficient monolithic perovskite/silicon tandem solar cell with cell area > 1 cm². J Phys Chem Lett 7:161–166. https://doi.org/10.1021/acs.jpclett.5b02686

30. Wu Y, Yan D, Peng J et al (2017) Monolithic perovskite/silicon-homojunction tandem solar cell with over 22% efficiency. Energy Environ Sci 10:2472–2479. https://doi.org/10.1039/c7ee02288c

31. Xu J, Boyd CC, Yu ZJ et al (2020) Triple-halide wide-band gap perovskites with suppressed phase segregation for efficient tandems. Science 367:1097–1104. https://doi.org/10.1126/science.aaz5074

32. Zheng J, Lau CFJ, Mehrvarz H et al (2018) Large area efficient interface layer free monolithic perovskite/homo-junction-silicon tandem solar cell with over 20% efficiency. Energy Environ Sci 11:2432–2443. https://doi.org/10.1039/c8ee00689j

33. Zheng J, Mehrvarz H, Liao C, Bing J, Cui X, Li Y, Gonçales VR, Lau CFJ, Lee DS, Li Y, Zhang M, Kim J, Cho Y, Caro LG, Tang S, Chen C, Huang S, Ho-Baillie AWY (2019) Large-area 23%-efficient monolithic perovskite/homojunction-silicon tandem solar cell with enhanced uv stability using down-shifting material. ACS Energy Lett 4(11):2623–2631. https://doi.org/10.1021/acsenergylett.9b01783

34. Zheng J, Mehrvarz H, Ma F-J, Lau CFJ, Green MA, Huang S, Ho-Baillie AWY (2018) 21.8% efficient monolithic perovskite/homojunction-silicon tandem solar cell on 16 cm². ACS Energy Lett 3(9):2299–2300. https://doi.org/10.1021/acsenergylett.8b01382

35. Zhu S, Hou F, Huang W et al (2018) Solvent engineering to balance light absorbance and transmittance in perovskite for tandem solar cells. Sol RRL 2:1800176. https://doi.org/10.1002/solr.201800176

36. Zhu S, Yao X, Ren Q et al (2018) Transparent electrode for monolithic perovskite/silicon-heterojunction two-terminal tandem solar cells. Nano Energy 45:280–286. https://doi.org/10.1016/j.nanoen.2017.12.043

37. Hou F, Li Y, Yan L et al (2021) Control perovskite crystals vertical growth for obtaining high-performance monolithic perovskite/silicon heterojunction tandem solar cells with V_{OC} of 1.93 V. Sol RRL 5:2100357. https://doi.org/10.1002/solr.202100357

38. Kamino BA, Paviet-Salomon B, Moon S-J et al (2019) Low-temperature screen-printed metallization for the scale-up of two-terminal perovskite-silicon tandems. ACS Appl Energy Mater 2:3815–3821. https://doi.org/10.1021/acsaem.9b00502

39. Aydin E, Liu J, Ugur E et al (2021) Ligand-bridged charge extraction and enhanced quantum efficiency enable efficient n-i-p perovskite/silicon tandem solar cells. Energy Environ Sci 14:4377–4390. https://doi.org/10.1039/d1ee01206a

40. Chen B, Yu ZJ, Manzoor S, Wang S, Weigand W, Yu Z, Yang G, Ni Z, Dai X, Holman ZC, Huang J (2020) Blade-coated perovskites on textured silicon for 26%-efficient monolithic perovskite/silicon tandem solar cells. Joule 4(4):850–864. https://doi.org/10.1016/j.joule.2020.01.008

41. De Bastiani M, Mirabelli AJ, Hou Y et al (2021) Efficient bifacial monolithic perovskite/silicon tandem solar cells via bandgap engineering. Nat Energy 6:167–175. https://doi.org/10.1038/s41560-020-00756-8

42. Hou Y, Aydin E, De Bastiani M et al (2020) Efficient tandem solar cells with solution-processed perovskite on textured crystalline silicon. Science 367:1135–1140. https://doi.org/10.1126/science.aaz3691

43. Isikgor FH, Furlan F, Liu J et al (2021) Concurrent cationic and anionic perovskite defect passivation enables 27.4% perovskite/silicon tandems with suppression of halide segregation. Joule 5:1566–1586. https://doi.org/10.1016/j.joule.2021.05.013

44. Subbiah AS, Isikgor FH, Howells CT et al (2020) High-performance perovskite single-junction and textured perovskite/silicon tandem solar cells via slot-die-coating. ACS Energy Lett 5:3034–3040. https://doi.org/10.1021/acsenergylett.0c01297

45. Zhumagali S, Isikgor FH, Maity P, Yin J, Ugur E, de Bastiani M, Subbiah AS, Mirabelli AJ, Azmi R, Harrison GT, Troughton J, Aydin E, Liu J, Allen T, Rehman A, Baran D, Mohammed OF, de Wolf S (2021) Linked nickel oxide/

46. Nogay G, Sahli F, Werner J, Monnard R, Boccard M, Despeisse M, Haug FJ, Jeangros Q, Ingenito A, Ballif C (2019) 25.1%-efficient monolithic perovskite/silicon tandem solar cell based on a p-type monocrystalline textured silicon wafer and high-temperature passivating contacts. ACS Energy Lett 4(4):844–845. https://doi.org/10.1021/acsenergylett.9b00377

47. Ross M, Severin S, Stutz MB et al (2021) Co-evaporated formamidinium lead iodide based perovskites with 1000 h constant stability for fully textured monolithic perovskite/silicon tandem solar cells. Adv Energy Mater 11:2101460. https://doi.org/10.1002/aenm.202101460

48. Sahli F, Werner J, Kamino BA, Bräuninger M, Monnard R, Paviet-Salomon B, Barraud L, Ding L, Diaz Leon JJ, Sacchetto D, Cattaneo G, Despeisse M, Boccard M, Nicolay S, Jeangros Q, Niesen B, Ballif C (2018) Fully textured monolithic perovskite/silicon tandem solar cells with 25.2% power conversion efficiency. Nat Mater 17(9):820–826. https://doi.org/10.1038/s41563-018-0115-4

49. Lamanna E, Matteocci F, Calabro E et al (2020) Mechanically stacked, two-terminal graphene-based perovskite/silicon tandem solar cell with efficiency over 26%. Joule 4:865–881. https://doi.org/10.1016/j.joule.2020.01.015

50. National Renewable Energy Laboratory (NREL), Best research-cell efficiency chart (2021) https://www.nrel.gov/pv/cell-efficiency.html

51. Lee JW, Hsieh YT, De Marco N et al (2017) Halide perovskites for tandem solar cells. J Phys Chem Lett 8:1999–2011. https://doi.org/10.1021/acs.jpclett.7b00374

52. Todorov TK, Bishop DM, Lee YS (2018) Materials perspectives for next-generation low-cost tandem solar cells. Sol Energy Mater Sol Cells 180:350–357. https://doi.org/10.1016/j.solmat.2017.07.033

53. Werner J, Niesen B, Ballif C (2017) Perovskite/silicon tandem solar cells: marriage of convenience or true love story?–An overview. Adv Mater Interfaces 5:1700731. https://doi.org/10.1002/admi.201700731

54. Sha WEI, Ren X, Chen L et al (2015) The efficiency limit of CH₃NH₃PbI₃ perovskite solar cells. Appl Phys Lett 106:221104. https://doi.org/10.1063/1.4922150

55. De Vos A (1980) Detailed balance limit of the efficiency of tandem solar cells. J Phys D 13:839–846. https://doi.org/10.1088/0022-3727/13/5/018

56. Brown AS, Green MA (2002) Limiting efficiency for current-constrained two-terminal tandem cell stacks. Prog Photovoltaics 10:299–307. https://doi.org/10.1002/pip.425

57. Zhang H, Shi Z, Hu L, Tang YY, Qin Z, Liao WQ, Wang ZS, Qin J, Li X, Wang H, Gusain M, Liu F, Pan Y, Xu M, Wang J, Liu R, Zhang C, Xiong RG, Sha WEI, Zhan Y (2021) Highly efficient 1D/3D ferroelectric perovskite solar cell. Adv Funct Mater 31(27):2100205. https://doi.org/10.1002/adfm.202100205

58. Li H, Zhang W (2020) Perovskite tandem solar cells: from fundamentals to commercial deployment. Chem Rev 120:9835–9950. https://doi.org/10.1021/acs.chemrev.9b00780

59. Byers JC, Ballantyne S, Rodionov K, Mann A, Semenikhin OA (2011) Mechanism of recombination losses in bulk heterojunction P3HT:PCBM solar cells studied using intensity modulated photocurrent spectroscopy. ACS Appl Mater Interfaces 3(2):392–401. https://doi.org/10.1021/am100998t

60. Létay G, Hermle M, Bett AW (2006) Simulating single-junction GaAs solar cells including photon recycling. Prog Photovoltaics 14(8):683–696. https://doi.org/10.1002/pip.699

61. Li P, Xiong H, Lin L et al (2021) Modeling and simulation of bifacial perovskite/PERT-silicon tandem solar cells. Sol Energy 227:292–302. https://doi.org/10.1016/j.solener.2021.09.015

62. Ba L, Liu H, Shen W (2018) Perovskite/c-Si tandem solar cells with realistic inverted architecture: achieving high efficiency by optical optimization. Prog Photovoltaics 26:924–933. https://doi.org/10.1002/pip.3037

63. Hossain MI, Qarony W, Ma S et al (2019) Perovskite/silicon tandem solar cells: from detailed balance limit calculations to photon management. Nanomicro Lett 11:58. https://doi.org/10.1007/s40820-019-0287-8

64. Jäger K, Sutter J, Hammerschmidt M, Schneider PI, Becker C (2021) Prospects of light management in perovskite/silicon tandem solar cells. Nanophotonics 10(8):1991–2000. https://doi.org/10.1515/nanoph-2020-0674

65. Zandi S, Razaghi M (2019) Finite element simulation of perovskite solar cell: a study on efficiency improvement based on structural and material modification. Sol Energy 179:298–306. https://doi.org/10.1016/j.solener.2018.12.032

66. Archambeault B, Ramahi OM, Brench C (1998) Method of moments. In: EMI/ EMC computational modeling handbook. Springer, Boston, pp 69–82. https://doi.org/10.1007/978-1-4757-5124-6_4

67. Ba L, Wang T, Wang J, Shen W (2019) Perovskite/c-Si monolithic tandem solar cells under real solar spectra: improving energy yield by oblique incident optimization. J Phys Chem C 123(47):28659–28667. https://doi.org/10.1021/acs.jpcc.9b10186

68. Qarony W, Hossain MI, Jovanov V et al (2020) Influence of perovskite interface morphology on the photon management in perovskite/silicon tandem solar cells. ACS Appl Mater Interfaces 12:15080–15086. https://doi.org/10.1021/acsami.9b21985

69. Shi D, Zeng Y, Shen W (2015) Perovskite/c-Si tandem solar cell with inverted nanopyramids: realizing high efficiency by controllable light trapping. Sci Rep 5(1):16504. https://doi.org/10.1038/srep16504

70. Tennyson EM, Frohna K, Drake WK et al (2021) Multimodal microscale imaging of textured perovskite-silicon tandem solar cells. ACS Energy Lett 6: 2293–2304. https://doi.org/10.1021/acsenergylett.1c00568

71. Wang J, Gao C, Wang X, Wang Y, Cheng Z, Liu H, Shen W (2020) Simple solution-processed approach for nanoscale coverage of perovskite on textured silicon surface enabling highly efficient perovskite/Si tandem solar cells. Energy Technol 9(1):2000778. https://doi.org/10.1002/ente.202000778

72. Bittkau K, Kirchartz T, Rau U (2018) Optical design of spectrally selective interlayers for perovskite/silicon heterojunction tandem solar cells. Opt Express 26:750–760. https://doi.org/10.1364/oe.26.00a750

73. Cherif FE, Sammouda H (2020) Strategies for high performance perovskite/c-Si tandem solar cells: effects of bandgap engineering, solar concentration and device temperature. Opt Mater 106:109935. https://doi.org/10.1016/j.optmat.2020.109935

74. Zhang L, Xie Z, Tian F, Qin G (2017) Simulation calculations of efficiencies and silicon consumption for $CH_3NH_3PbI_{3-x-y}Br_xCl_y$/crystalline silicon tandem solar cells. J Phys D 50(15):155102. https://doi.org/10.1088/1361-6463/aa5f7f

75. Zhao P, Hao Y, Yue M et al (2018) Device simulation of organic-inorganic halide perovskite/crystalline silicon four-terminal tandem solar cell with various antireflection materials. IEEE J Photovolt 8:1685–1691. https://doi.org/10.1109/jphotov.2018.2869743

76. Li J, Monk P, Weile D (2015) Time domain integral equation methods in computational electromagnetism. In: Computational electromagnetism. Springer, Cetraro, pp 111–189

77. Shang A, Li X (2017) Photovoltaic devices: opto-electro-thermal physics and modeling. Adv Mater 29:1603492. https://doi.org/10.1002/adma.201603492

78. An Y, Wang C, Cao G et al (2020) Heterojunction perovskite solar cells: opto-electro-thermal physics, modeling, and experiment. ACS Nano 14:5017–5026. https://doi.org/10.1021/acsnano.0c01392

79. Green MA (1982) Generation, recombination, and the basic equations of device physics. In: Solar cells: operating principles, technology, and system applications. Prentice-Hall, New Jersey, pp 56–58

80. Abdelraouf OAM, Allam NK (2016) Towards nanostructured perovskite solar cells with enhanced efficiency: coupled optical and electrical modeling. Sol Energy 137:364–370. https://doi.org/10.1016/j.solener.2016.08.039

81. Munday JN, Atwater HA (2011) Large integrated absorption enhancement in plasmonic solar cells by combining metallic gratings and antireflection coatings. Nano Lett 11(6):2195–2201. https://doi.org/10.1021/nl101875t

82. Onno A, Rodkey N, Asgharzadeh A et al (2020) Predicted power output of silicon-based bifacial tandem photovoltaic systems. Joule 4:580–596. https://doi.org/10.1016/j.joule.2019.12.017

83. Pandey R, Chaujar R (2016) Numerical simulations: toward the design of 27.6% efficient four-terminal semi-transparent perovskite/SiC passivated rear contact silicon tandem solar cell. Superlattice Microst 100:656–666. https://doi.org/10.1016/j.spmi.2016.10.033

84. Du D, Gao C, Wang H et al. Photovoltaic performance of bifacial perovskite/ c-Si tandem solar cells In submission

85. Liu Z, Ren Z, Liu H et al (2017) A modeling framework for optimizing current density in four-terminal tandem solar cells: a case study on GaAs/Si tandem. Sol Energy Mater Sol Cells 170:167–177. https://doi.org/10.1016/j.solmat.2017.05.048

86. Eisenlohr J, Tucher N, Hohn O et al (2015) Matrix formalism for light propagation and absorption in thick textured optical sheets. Opt Express 23: 502–518. https://doi.org/10.1364/OE.23.00A502

87. Li Y, Chen Y, Ouyang Z, Lennon A (2015) Angular matrix framework for light trapping analysis of solar cells. Opt Express 23(24):1707–1719. https://doi.org/10.1364/OE.23.0A1707

88. Tucher N, Eisenlohr J, Gebrewold H et al (2016) Optical simulation of photovoltaic modules with multiple textured interfaces using the matrix-based formalism OPTOS. Opt Express 24:1083–1093. https://doi.org/10.1364/OE.24.0A1083

89. Tucher N, Eisenlohr J, Kiefel P, Höhn O, Hauser H, Peters M, Müller C, Goldschmidt JC, Bläsi B (2015) 3D optical simulation formalism OPTOS for textured silicon solar cells. Opt Express 23(24):1720–1734. https://doi.org/10.1364/OE.23.0A1720

90. Tucher N, Hohn O, Goldschmidt JC et al (2018) Optical modeling of structured silicon-based tandem solar cells and module stacks. Opt Express 26(18):761–768. https://doi.org/10.1364/OE.26.00A761

91. MacQueen RW, Liebhaber M, Niederhausen J et al (2018) Crystalline silicon solar cells with tetracene interlayers: the path to silicon-singlet fission heterojunction devices. Mater Horizons 5:1065–1075. https://doi.org/10.1039/c8mh00853a

92. Santbergen R, Meguro T, Suezaki T et al (2017) GenPro4 optical model for solar cell simulation and its application to multijunction solar cells. IEEE J Photovolt 7:919–926. https://doi.org/10.1109/jphotov.2017.2669640

93. Schneider BW, Lal NN, Baker-Finch S et al (2014) Pyramidal surface textures for light trapping and antireflection in perovskite-on-silicon tandem solar cells. Opt Express 22:1422–1430. https://doi.org/10.1364/OE.22.0A1422

94. Onno A, Harder N-P, Oberbeck L, Liu H (2016) Simulation study of GaAsP/Si tandem solar cells. Sol Energy Mater Sol Cells 145:206–216. https://doi.org/10.1016/j.solmat.2015.10.028

95. Timò G, Martinelli A, Andreani LC (2020) A new theoretical approach for the performance simulation of multijunction solar cells. Prog Photovoltaics 28: 279–294. https://doi.org/10.1002/pip.3225

96. Yu M, Li Y, Cheng Q, Li S (2019) Numerical simulation of graphene/GaAs heterojunction solar cells. Sol Energy 182:453–461. https://doi.org/10.1016/j.solener.2019.02.061

97. Kojima A, Teshima K, Shirai Y, Miyasaka T (2009) Organometal halide perovskites as visible-light sensitizers for photovoltaic cells. J Am Chem Soc 131(17):6050–6051. https://doi.org/10.1021/ja809598r

98. Min H, Lee DY, Kim J, Kim G, Lee KS, Kim J, Paik MJ, Kim YK, Kim KS, Kim MG, Shin TJ, Il Seok S (2021) Perovskite solar cells with atomically coherent interlayers on SnO_2 electrodes. Nature 598(7881):444–450. https://doi.org/10.1038/s41586-021-03964-8

99. Hao F, Stoumpos CC, Chang RP et al (2014) Anomalous band gap behavior in mixed Sn and Pb perovskites enables broadening of absorption spectrum in solar cells. J Am Chem Soc 136:8094–8099. https://doi.org/10.1021/ja5033259

100. Ma T, Wang S, Zhang Y et al (2019) The development of all-inorganic $CsPbX_3$ perovskite solar cells. J Mater Sci 55:464–479. https://doi.org/10.1007/s10853-019-03974-y

101. Noh JH, Im SH, Heo JH et al (2013) Chemical management for colorful, efficient, and stable inorganic-organic hybrid nanostructured solar cells. Nano Lett 13:1764–1769. https://doi.org/10.1021/nl400349b

102. Li B, Ferguson V, Silva SRP et al (2018) Defect engineering toward highly efficient and stable perovskite solar cells. Adv Mater Interfaces 5:1800326. https://doi.org/10.1002/admi.201800326

103. Poindexter JR, Hoye RLZ, Nienhaus L et al (2017) High tolerance to iron contamination in lead halide perovskite solar cells. ACS Nano 11:7101–7109. https://doi.org/10.1021/acsnano.7b02734

104. De Wolf S, Holovsky J, Moon SJ et al (2014) Organometallic halide perovskites: sharp optical absorption edge and its relation to photovoltaic performance. J Phys Chem Lett 5:1035–1039. https://doi.org/10.1021/jz500279b

105. Min H, Kim M, Lee SU et al (2019) Efficient, stable solar cells by using inherent bandgap of alpha-phase formamidinium lead iodide. Science 366: 749–753. https://doi.org/10.1126/science.aay7044

106. Wang T, Ding D, Zheng H et al (2019) Efficient inverted planar perovskite solar cells using ultraviolet/ozone-treated NiO_x as the hole transport layer. Sol RRL 3:1900045. https://doi.org/10.1002/solr.201900045

107. Woo MY, Choi K, Lee JH et al (2021) Recent progress in the semiconducting oxide overlayer for halide perovskite solar cells. Adv Energy Mater 11: 2003119. https://doi.org/10.1002/aenm.202003119

108. Chen Q, Zhou H, Hong Z, Luo S, Duan HS, Wang HH, Liu Y, Li G, Yang Y (2014) Planar heterojunction perovskite solar cells via vapor-assisted solution process. J Am Chem Soc 136(2):622–625. https://doi.org/10.1021/ja411509g

109. Cheng Z, Gao C, Song J et al (2021) Interfacial and permeating modification effect of n-type non-fullerene acceptors toward high-performance

perovskite solar cells. ACS Appl Mater Interfaces 13:40778–40787. https://doi.org/10.1021/acsami.1c13447

110. Liu M, Johnston MB, Snaith HJ (2013) Efficient planar heterojunction perovskite solar cells by vapour deposition. Nature 501:395–398. https://doi.org/10.1038/nature12509

111. Luo D, Zhao L, Wu J, Hu Q, Zhang Y, Xu Z, Liu Y, Liu T, Chen K, Yang W, Zhang W, Zhu R, Gong Q (2017) Dual-source precursor approach for highly efficient inverted planar heterojunction perovskite solar cells. Adv Mater 29(19):1604758. https://doi.org/10.1002/adma.201604758

112. Li Y, Zhong S, Zhuang Y, Yang L, Meng F, Wang W, Li Z, Shen W (2019) Quasi-omnidirectional ultrathin silicon solar cells realized by industrially compatible processes. Adv Electron Mater 5(3):1800858. https://doi.org/10.1002/aelm.201800858

113. Zhong S, Dreon J, Jeangros Q et al (2019) Mitigating plasmonic absorption losses at rear electrodes in high-efficiency silicon solar cells using dopant-free contact stacks. Adv Funct Mater 30:1907840. https://doi.org/10.1002/adfm.201907840

114. Xu CY, Hu W, Wang G et al (2020) Coordinated optical matching of a texture interface made from demixing blended polymers for high-performance inverted perovskite solar cells. ACS Nano 14:196–203. https://doi.org/10.1021/acsnano.9b07594

115. Manzoor S, Yu ZJ, Ali A et al (2017) Improved light management in planar silicon and perovskite solar cells using PDMS scattering layer. Sol Energy Mater Sol Cells 173:59–65. https://doi.org/10.1016/j.solmat.2017.06.020

116. Lv Y, Zhuang YF, Wang WJ, Wei WW, Sheng J, Zhang S, Shen WZ (2020) Towards high-efficiency industrial p-type mono-like Si PERC solar cells. Sol Energy Mater Sol Cells 204:110202. https://doi.org/10.1016/j.solmat.2019.110202

117. Tang HB, Ma S, Lv Y et al (2020) Optimization of rear surface roughness and metal grid design in industrial bifacial PERC solar cells. Sol Energy Mater Sol Cells 216:110712. https://doi.org/10.1016/j.solmat.2020.110712

118. Zhuang YF, Zhong SH, Liang XJ et al (2019) Application of SiO$_2$ passivation technique in mass production of silicon solar cells. Sol Energy Mater Sol Cells 193:379–386. https://doi.org/10.1016/j.solmat.2019.01.038

119. Santbergen R, Mishima R, Meguro T et al (2016) Minimizing optical losses in monolithic perovskite/c-Si tandem solar cells with a flat top cell. Opt Express 24:1288–1299. https://doi.org/10.1364/OE.24.0A1288

120. Jacobs DA, Langenhorst M, Sahli F, Richards BS, White TP, Ballif C, Catchpole KR, Paetzold UW (2019) Light management: a key concept in high-efficiency perovskite/silicon tandem photovoltaics. J Phys Chem Lett 10(11):3159–3170. https://doi.org/10.1021/acs.jpclett.8b03721

121. Ding D, Lu G, Li Z, Zhang Y, Shen W (2019) High-efficiency n-type silicon PERT bifacial solar cells with selective emitters and poly-Si based passivating contacts. Sol Energy 193:494–501. https://doi.org/10.1016/j.solener.2019.09.085

122. Guerrero-Lemus R, Vega R, Kim T, Kimm A, Shephard LE (2016) Bifacial solar photovoltaics - a technology review. Renew Sust Energ Rev 60:1533–1549. https://doi.org/10.1016/j.rser.2016.03.041

123. Patel MT, Vijayan RA, Asadpour R et al (2020) Temperature-dependent energy gain of bifacial PV farms: a global perspective. Appl Energy 276:115405. https://doi.org/10.1016/j.apenergy.2020.115405

124. Liang TS, Pravettoni M, Deline C et al (2019) A review of crystalline silicon bifacial photovoltaic performance characterisation and simulation. Energy Environ Sci 12:116–148. https://doi.org/10.1039/c8ee02184h

125. 11th edition of the international technology roadmap photovoltaics (ITRPV) (2020) https://itrpv.vdma.org

126. Chantana J, Kawano Y, Nishimura T, Mavlonov A, Minemoto T (2021) Optimized bandgaps of top and bottom subcells for bifacial two-terminal tandem solar cells under different back irradiances. Sol Energy 220:163–174. https://doi.org/10.1016/j.solener.2021.03.034

127. Lehr J, Langenhorst M, Schmager R et al (2020) Energy yield of bifacial textured perovskite/silicon tandem photovoltaic modules. Sol Energy Mater Sol Cells 208:110367. https://doi.org/10.1016/j.solmat.2019.110367

128. Hanmandlu C, Chen CY, Boopathi KM et al (2017) Bifacial perovskite solar cells featuring semitransparent electrodes. ACS Appl Mater Interfaces 9:32635–32642. https://doi.org/10.1021/acsami.7b06607

129. Pang S, Chen D, Zhang C et al (2017) Efficient bifacial semitransparent perovskite solar cells with silver thin film electrode. Sol Energy Mater Sol Cells 170:278–286. https://doi.org/10.1016/j.solmat.2017.05.071

130. Jäger K, Tillmann P, Katz EA et al (2021) Perovskite/silicon tandem solar cells: effect of luminescent coupling and bifaciality. Sol RRL 5:2000628. https://doi.org/10.1002/solr.202000628

131. Du DX, Gao C, Zhang DZ et al (2021) Low-cost strategy for high-efficiency bifacial perovskite/c-Si tandem solar cells. Sol RRL:2100781. https://doi.org/10.1002/solr.202100781

132. Hörantner MT, Snaith HJ (2017) Predicting and optimising the energy yield of perovskite-on-silicon tandem solar cells under real world conditions. Energy Environ Sci 10(9):1983–1993. https://doi.org/10.1039/c7ee01232b

133. Boccard M, Ballif C (2020) Influence of the subcell properties on the fill factor of two-terminal perovskite-silicon tandem solar cells. ACS Energy Lett 5(4):1077–1082. https://doi.org/10.1021/acsenergylett.0c00156

134. Futscher MH, Ehrler B (2017) Modeling the performance limitations and prospects of perovskite/Si tandem solar cells under realistic operating conditions. ACS Energy Lett 2:2089–2095. https://doi.org/10.1021/acsenergylett.7b00596

135. Qian J, Thomson AF, Wu Y et al (2018) Impact of perovskite/silicon tandem module design on hot-spot temperature. ACS Appl Energy Mater 1:3025–3029. https://doi.org/10.1021/acsaem.8b00480

136. Futscher MH, Ehrler B (2016) Efficiency limit of perovskite/Si tandem solar cells. ACS Energy Lett 1:863–868. https://doi.org/10.1021/acsenergylett.6b00405

137. Tucher N, Hohn O, Murthy JN et al (2019) Energy yield analysis of textured perovskite silicon tandem solar cells and modules. Opt Express 27:1419–1430. https://doi.org/10.1364/OE.27.0A1419

138. Schmager R, Langenhorst M, Lehr J et al (2019) Methodology of energy yield modelling of perovskite-based multi-junction photovoltaics. Opt Express 27:507–523. https://doi.org/10.1364/OE.27.00A507

139. Julien A, Puel JB, Lopez-Varo P, Guillemoles JF, Collin S (2020) Backside light management of 4-terminal bifacial perovskite/silicon tandem PV modules evaluated under realistic conditions. Opt Express 28(25):37487–37504. https://doi.org/10.1364/OE.405713

140. Zhang Y, Yu Y, Meng F, Liu Z (2020) Experimental investigation of the shading and mismatch effects on the performance of bifacial photovoltaic modules. IEEE J Photovolt 10(1):296–305. https://doi.org/10.1109/jphotov.2019.2949766

141. Li Y, Shi B, Xu Q et al (2021) Wide bandgap interface layer induced stabilized perovskite/silicon tandem solar cells with stability over ten thousand hours. Adv Energy Mater:2102046. https://doi.org/10.1002/aenm.202102046

Publisher's Note